HHS Public Access

Author manuscript

Adv Mater. Author manuscript; available in PMC 2025 February 01.

Published in final edited form as:

Adv Mater. 2024 February ; 36(7): e2304759. doi:10.1002/adma.202304759.

Synchronous and Fully Steerable Active Particle Systems for Enhanced Mimicking of Collective Motion in Nature

Zhihan Chen[1], **Hongru Ding**[2], **Pavana Siddhartha Kollipara**[2], **Jingang Li**[1], **Yuebing Zheng**[1,2]

[1]Materials Science & Engineering Program and Texas Materials Institute, The University of Texas at Austin, Austin, TX 78712, USA.

[2]Walker Department of Mechanical Engineering, The University of Texas at Austin, Austin, TX 78712, USA.

Abstract

The collective motion observed in living active matter, such as fish schools and bird flocks, is characterized by its dynamic and complex nature, involving various moving states and transitions. By tailoring physical interactions or incorporating information exchange capabilities, inanimate active particles can exhibit similar behavior. However, the lack of synchronous and arbitrary control over individual particles hinders their use as a test system for the study of more intricate collective motions in living species. Herein, we propose a novel optical feedback control system that enables the mimicry of collective motion observed in living objects using active particles. This system allows for the experimental investigation of the velocity alignment, a seminal model of collective motion (known as the Vicsek model), in a microscale perturbed environment with controllable and realistic conditions. We observe the spontaneous formation of different moving states and dynamic transitions between these states. Additionally, we quantitatively validate the high robustness of the active-particle group at the critical density under the influence of different perturbations. Our findings support the effectiveness of velocity alignment in real perturbed environments, thereby providing a versatile platform for fundamental studies on collective motion and the development of innovative swarm microrobotics.

Graphical Abstract

zheng@austin.utexas.edu .

Author Contributions: Z.C. and Y.Z. conceived the idea for this study. Z.C. performed all the experiments and simulations, including the writing of LabVIEW and MATLAB codes. H.D. offered the recipe and control method of the active particle system. P.K. helped with the MATLAB codes and the modeling of single-particle propulsion. J.L. helped to proofread and revise the manuscript. Y.Z. supervised the project. Z.C. and Y.Z. wrote the manuscript with the input of all other authors. All authors approved the manuscript.

Competing Interest Statement: The authors declare no competing interests.

Supporting Information

Supporting Information is available from the Wiley Online Library or from the author.

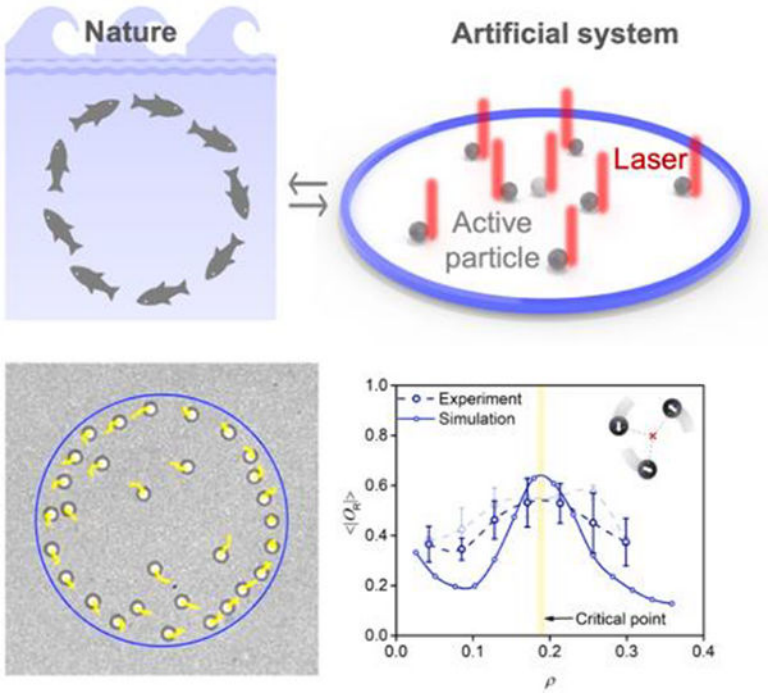

A novel active-particle experimental platform is developed to imitate collective motion observed in nature. Fully synchronous and arbitrary navigation of active particles are implemented at individual level. Particle motion is regulated by the bio-inspired velocity alignment rule and long-range physical interaction. Density-dependent state-transition and high robustness to noisy environments are observed experimentally in a controllable and realistic manner.

Keywords

collective motions; active particles; optical manipulation; feedback control; velocity alignment

1. Introduction

Collective motion[1] is a prevalent phenomenon observed in various living systems across different scales, ranging from fish schools[2] and bird flocks[3] to bacteria[4] and subcellular molecular motors.[5] These systems exhibit diverse moving patterns, including disordered swarms,[6] polar flocks,[7] and vortex groups (also known as rotating, swirling, or milling states).[8] Density-dependent collective behaviors and transitions between different moving patterns have also been observed in these systems.[8a, 9] Understanding the complex and dynamic behaviors of collective motions in nature not only sheds light on the functioning of living objects as a group but also advances the field of robotics. the two traditional approaches - direct observation and analysis of collective motions in nature[10] and pure theories and analytical models,[11] -suffer from the limitations of excessive (and occasionally uncontrollable) variables in natural environments and oversimplified conditions that deviate from reality, respectively.

To investigate collective motion in a controllable and realistic manner, as well as to develop swarm robotics, researchers have explored the use of macroscopic robots[12] and active particles. Active particles are nonequilibrium entities that consume energy for persistent self-propulsion at micro- or nanoscale,[13] which can mimic and probe the collective motion of living objects. Various approaches have been employed, such as active particles powered by magnetic,[14] electric,[15] chemical,[16] and defocused light fields.[17] Though featuring simultaneous actuation of numerous particles, the global nature of these applied fields lacks the capability to replicate the individual-level intelligence found in the living organisms.

In contrast, active particles driven by focused optical fields can be individually manipulated by dynamically adjusting spatial light patterns. By leveraging feedback control, these active particles can possess sensing and information processing capabilities so that each one can adjust its motion by sensing its own environmental conditions,[18] resembling the behavior of living objects. This approach has been utilized to investigate quorum sensing,[19] visual-perception-dependent mobility,[20] vortex formation,[21] and the impact of changing interaction rules[22] or environmental threats.[23] However, existing active-particle experimental systems using focused optical fields suffer from limitations, including poor reorientation capability of particles,[19–21, 22–23] a limited number of manipulated particles,[18, 20] and asynchronous control among different particles.[18–23] These limitations prevent the investigation of more general collective behaviors in nature and hinder the development of efficient microrobotic swarms, since the majority of living species feature fast reorientation and exhibit collective motion when there is a relatively large number of group members.[11a–c]

To address these challenges and advance the field, we have developed a new optical feedback control system that enables fully synchronous and arbitrary navigation of active particles, which lead to active particles behaving more like living objects. This system facilitates the first experimental study of the Vicsek model, a seminal model in collective motion that focuses on velocity alignment, at the microscale level. We successfully reproduced density-dependent collective motion of active particles, even in the presence of various perturbations, which exactly reflects what has been observed in some of living species (e.g., fishes[8a] and locusts[9]). Our approach combines velocity-alignment-based information exchange with long-range physical interactions, resulting in ordered collective movement and state transitions with a critical transition point in the particle density (i.e., critical density point). Surprisingly, we discovered that, Brownian motion and particle heterogeneity significantly increase the frequency of state switching around the critical density point while having limited influence on the robustness of collective structures. Furthermore, we experimentally demonstrated popular variants of the Vicsek model, including topological distance[24] and different-shaped confined geometries[25] based on our integrated platform.

2. Programmable feedback control platform

Our platform, which enables autonomous control of active particles based on interaction rules extracted from collective motions in nature, can be divided into four distinct parts (Figure 1A). First, each of the active particles within the algorithm-defined confined

geometry is individually and persistently propelled by their own exclusive laser beams, which are placed around their circumferences. Simultaneously, the spatiotemporal positions of all particles are detected by the camera, where the real-time position and velocity of each particle are extracted and then fed to the control algorithm. Thereafter, the control algorithm will process the information based on the predefined model and then solve the new positions of the laser beams for each particle. Next, corresponding holograms are calculated and transferred to the spatial light modulator (SLM) to modulate the input single laser beam into a diffracted laser pattern. Finally, each particle is propelled in its own new direction, starting the next feedback loop (Methods and Figure S1). Compared with acousto-optic deflectors used in all the previous setups that fast scan a single laser beam to control the particles,[18–23] SLM can diffract one laser beam into multiple beams with arbitrary number and positions to independently trigger the motion of different particles, ensuring synchronous control in our platform.

In this study, we utilize the classic Vicsek model to describe the non-physical interaction among particles. Furthermore, we incorporate the long-range physical interaction between particles into the Vicsek model. Such long-range interaction is specific to the active-particle manipulation technique used in our platform.[26] Accordingly, different from the classic Vicsek model,[11c] our new model features particle's velocity being determined by the average velocity direction of the particle and its neighboring ones[11c] under the influence of additional long-range physical interaction:

$$\theta_j^{t+\Delta t_0} = \arg\left[\sum_{k \in C_j} \left(\exp i(\theta_k^t + \phi_k^t + \delta_k^t)\right)\right] \quad (1)$$

$\theta_j^{t+\Delta t_0}$ is the new direction of particle j at time $t + \Delta t_0$ with Δt_0 being the timestep for one loop, C_j represents the circular neighborhood (radius r_0) of particle j, while θ_k^t, ϕ_k^t, and δ_k^t are the angles related to the velocity-alignment rule, the long-range physical interaction, and the Brownian motion of the k^{th} particle at time t (Figure S4), respectively. Note that only θ_k^t is actively controlled in our system to determine the laser position for each particle. ϕ_k^t is related to the long-range physical interaction and naturally decided after setting θ_k^t for every particle (Methods and Figure S4). Meanwhile, δ_k^t stems from the inherent Brownian motion of each particle, which is like the noise term in the classic Vicsek model. It should be noted that ϕ_k^t and δ_k^t vary across different active particles due to particle heterogeneity (Methods and Figure S5). In addition, volume exclusion is incorporated into the model to prevent particle collision and steric interaction (Methods).[11a] Moreover, a circular virtual boundary with the radius r_b and reflective boundary condition[27] is added for two reasons (Methods): to maintain the cohesion of the group, and to imitate the confinement-assisted self-organization in nature.[28] In the following discussion, the parameters are set as $\Delta t_0 = 0.132$ s, $r_0 = 7.75$ μm, and $r_b = 20.0$ μm.

The active particles used in this work are unmodified silica microspheres, whose propulsion comes from the synergy of two optothermal forces.[26, 29] This active-particle system

provides two distinct advantages. First, compared with the commonly used Janus particles in many reported experimental setups,[19–21, 22–23] homogeneous particles demonstrate no rotational diffusion, which permits instantaneous change in their propulsion directions (See Supplementary Note 1). Second, due to the long-range optothermal forces (> 20 μm), the motion of each active particle is not only determined by velocity alignment with their neighbors but also by the neighboring laser beams. In our active-particle system, the long-range physical interaction can be regarded as additional repelling force between two particles. The force magnitude decreases with the increasing interparticle distance (See Supplementary Note 1). It is worth noting that the long-range physical interaction was also observed in some living systems such as fishes[30] and bacteria.[8c] Accordingly, our experimental setup provides an ideal platform to study both information exchange and physical interactions in the collective motion of living objects. Due to the wide applicability of our experimental system (Figure S1), the long-range physical interaction included here can also be easily modified or removed by using other focused-light-driven active particles.[18, 20] Based on these inputs, dynamic collective structures of multiple particles are clearly observed in experiments (Movie S1).

We first prove that the observed collective motion is indeed induced by velocity alignment rather than simply manipulating multiple particles in a predesigned vortex pattern. As shown in Figure 1B, when the velocity-alignment algorithm is removed, the group of particles only displays random motion (Movie S2). In contrast, the group of particles regulated by the velocity alignment shows stable rotation around the center of the geometry (Movie S3). We use two parameters[8a] to quantitatively describe the observed collective structure. One is the polarization order parameter (O_P) that measures the velocity alignment of the individuals in a group

$$O_P = \frac{1}{N}\left|\sum_{j=1}^{N} \boldsymbol{u}_j\right| \tag{2}$$

where N is the total number of particles, and $\boldsymbol{u}_j = (\cos\theta_j, \sin\theta_j)$. O_P has a value between 0 (no alignment) and 1 (perfect alignment). Another parameter, rotation order parameter (O_R), measures the degree of rotation about the center of the confined geometry

$$O_R = \frac{1}{N}\sum_{j=1}^{N} \boldsymbol{u}_j \times \boldsymbol{r}_j \tag{3}$$

where $\boldsymbol{r}_j$ is the vector from the center of the particle to the center of the confined geometry. O_R takes a value from −1 to 1. Its sign indicates the rotation direction, and its magnitude shows the strength of the rotation. Accordingly, we depict the time-varied O_P and O_R of the experimental realizations with and without velocity alignment (Figure 1C). The result shows the existence of polar alignment, stable rotation, and state transition among different collective states only within the velocity-alignment particle group, indicating that

the velocity-alignment rule plays an essential role in forming ordered collective structures here.

3. Quantification of perturbations

In the classic Vicsek model and its relevant derivatives, particles are usually assumed to be identical and propel at a constant speed. However, this assumption disables the model's depiction of living objects in the real world.[31] To overcome this limitation, we first quantify the velocity fluctuation and the heterogeneity in active particles that have been proved as non-negligible factors in natural collective motion.[32] An active particle with a laser beam at its edge must propel in the radial direction dictated by the laser propagation axis and the particle center. However, the inherent Brownian motion disturbs both the direction and magnitude of the propulsion velocity (Inset of Figure 2A). In addition, the unavoidable time delay arising from image acquisition and information processing in the feedback control makes the laser-particle distance (d) fluctuate within a small range,[33] which in-turn fluctuates the particles' velocities. To quantify the velocity and its fluctuation, two orthogonal velocity components are first precisely measured by experiment (Figure 2A), where the velocity induced by the laser ($|\boldsymbol{v}_{\text{laser}}|$) can then be extracted for certain optical density and d (See Supplementary Note 1.1). To further characterize the long-range physical interaction in our system, $|\boldsymbol{v}_{\text{laser}}|$ is also measured under different d to quantify the effect of one laser beam (associated with one particle) influencing the motion of its neighboring particles. The experimental data are fitted well by a force-inspired equation (Figure 2B and Supplementary Note 1.2), which is also input in our theoretical model to quantitatively discuss its influence. The slow decrease of $|\boldsymbol{v}_{\text{laser}}|$ as d increases validates that the long-range physical interaction plays a non-negligible role here. Moreover, we measured $\boldsymbol{v}_{\text{laser}}$ over 120 different silica particles (Figure 2C and Figure S5) to explicitly account for the heterogeneity of the particles through statistical analysis. This heterogeneity in motility mainly arises from the size and surface charge variation of colloidal particles, which corresponds to the individual difference among a group of living objects found in nature.[32b]

4. Analysis and modulation of collective motion

To understand how the velocity fluctuation and particle heterogeneity influence the collective motion in the real world, experiments under different particle densities are conducted with d and $|\boldsymbol{v}_{\text{laser}}|$ set as 0.93 μm and 1.34 μm s^{-1}, respectively. Here, we define particle density as $\rho = \frac{N*A_{\text{ve}}}{A_{\text{geometry}}}$ with N being the particle number, A_{ve} and A_{geometry} being the area of the single-particle repelling zone (defined by the volume exclusion radius r_{ve}) and the confined geometry, respectively. The selection of the volume-exclusion radius is a crucial factor in our study. If the radius is set too high, it can limit the effective working range of velocity alignment (Figure S6A) and lead to more frequent particle exclusions (Figure S6B), both of which can negatively impact the ordered collective motion. Conversely, if the volume exclusion radius is too low, it cannot guarantee collision-free behavior in real experiments. Therefore, we conducted simulations to determine the optimal volume-exclusion radius of $r_{\text{ve}} = 3.88$ μm (Figure S6C and S6D), striking a balance between

maintaining effective velocity alignment and ensuring collision avoidance. The experimental results show that, for $\langle|O_R|\rangle$, it first decreases at low density, then increases to a maximum, and finally declines again (Figure 3A). In contrast, $\langle O_P\rangle$ monotonically declines before gradually increasing at higher density (Figure 3B). Incorporating the above quantification of perturbations and long-range physical interaction, we establish a simulation model to probe the change of $\langle|O_R|\rangle$ and $\langle O_P\rangle$ (Methods). All the simulated results are averaged over 20 realizations and the value of each realization is obtained from the average value of the last half of an 8,000-timestep simulation, which ensures that the value represents the steady state of the collective structure. The simulation time for one realization and the number of realizations for average are determined by the convergence test (Methods and Figure S7). Figure 3A and 3B show an overall match between the experimental and simulation results.

To explain this density-dependent collective motion, we first show how the probability distribution of $|O_R|$ changes with the particle density (Figure 3C). At low-density region ($\rho < 0.1$), the broad peaks centered near $|O_R| \approx 0$ (Figure 3C) indicates that the collective structures within the low-density range are disordered swarms (Movie S4 and S5). The relatively high values of $\langle|O_R|\rangle$ and $\langle O_P\rangle$ around $\rho = 0.043$ can be mainly attributed to the finite-size effect (Figure S8). Our conclusion is further supported by the result without velocity alignment, which has the same $\langle|O_R|\rangle$ and $\langle O_P\rangle$ values at the low-density region compared to the case with velocity alignment (Figure S9). As the particle density increases ($\rho \geq 0.1$), stable collective motion starts to appear (Movie S1 and S4). A critical point at an intermediate particle density ($\rho \approx 0.19$) is observed, where the time-averaged state transition occurs between rotation and polarization. Thus, we have observed an interesting phenomenon in our study, wherein, above the critical density point, $\langle|O_R|\rangle$ decreases while $\langle O_P\rangle$ increases as the particle density raises (Figure 3A and 3B). This behavior can be attributed to the long-range physical interaction included in our current platform (Figure 2B). Specifically, the long-range physical interaction acts as an extra repelling force among particles, leading to the formation of a radial pattern in the collective structure. Initially, particles are pushed towards the boundary (Figure S10), and due to the reflective boundary condition (Methods), they start orbiting around the center of the confined geometry. These orbiting particles will contribute to the increase of $\langle|O_R|\rangle$ but result in a reduction of $\langle O_P\rangle$. On the contrary, the remaining particles stay inside the layer of orbiting particles (Figure S10), mainly contributing to the increase in $\langle O_P\rangle$ but decreasing $\langle|O_R|\rangle$. The reason is that the "boundary" for these inner particles is formed by the orbiting particles, which, unlike the reflective boundary condition, collectively exert a force to the inner particles, causing them to move towards the center of the confined geometry (Figure S10). Consequently, the inner particles tend to "bounce" within the orbiting-particle layer in a translational fashion (Figure S10), contributing to the increase of $\langle O_P\rangle$ but reducing $\langle|O_R|\rangle$. As particle density increases, the number of the orbiting particles near the boundary first increase but then almost saturate due to the volume exclusion rule (Methods), while the number of inner particles continues to increase. The opposing effects of the outer orbiting particles and the inner particles give rise to the emergence of a time-averaged state transition between rotation and polarization, accompanied by a corresponding critical density. In addition, the specific value of this critical density can be altered by the size of the geometry (Figure S8).

It is crucial to highlight again that this long-range physical interaction are not inherent to our experimental platform and can be easily modified or removed by using other types of focused-light-driven active particles.[18, 20] When the influence of long-range physical interaction is disregarded, equation (1) simplifies to the well-known Vicsek model in its classical form. The classic Vicsek model exhibits a phase transition between a disordered state and an ordered state, which is primarily determined by the system's density and noise.[11c] In our study, we observe a similar phase transition, where disordered swarms transform into rotating collective structures as the particle density increases (Movie S1 and S4). As the density further increases, we observe a distinct state transition from rotating-dominant collective structures to polar-dominant structures. We assume that this transition at the higher particle density is primarily driven by the presence of long-range physical interaction in our system. To validate this assumption, we have conducted simulations to show the disappearance of the state transition when the long-range repelling force is excluded (Figure S11, Movie S6 and S7).

As for the influence of different perturbations, the simulations reveal that Brownian motion and particle heterogeneity majorly lower the value of order parameters around the critical density but do not alter the shape of the curves (Figure S12). We also study the effect of instrumental uncertainty that stems from the particle-center detection error and the laser positioning error (Supplementary Note 2.1). Like other fluctuations, this uncertainty mainly lowers the order parameters around the critical density (Figure S2). Interestingly, in the experiment, we can actively reduce the influence of Brownian motion by increasing the time interval for the determination of the particle velocity. Specifically, we evaluate the particle velocity based on the initial and final positions in first and ninth image respectively, which alleviates the effect of Brownian motion and leads to more ordered collective structures (light dashed lines in Figure 3A and 3B). Additionally, the level of noise in the system can be adjusted by modifying the viscosity of the solution or changing the particle size (Movie S8 and Figure S13). Through the systematic adjustment, a noise-induced disorder-order transition has been observed in our experiments (Figure S13), which confirms that a sufficient noise range can be implemented in our platform for the investigation of collective motion. Overall, our collective structure at relatively high density can maintain a stable ordered movement, where the information-based velocity alignment guarantees the highly ordered structures under different perturbations while the long-range physical interaction introduces specific state transitions and critical behaviors to our system.

Remarkably, the spatiotemporal patterns of the collective structure are observed to switch back and forth in experiments even after reaching the steady state (Figure 4A), which is quite similar to the observations of fishes confined in a water tank[8a] or locusts in a ring-shaped arena.[9] Herein, this dynamical change in collective states is considered to stem from the reflective boundary and the perturbations (i.e., Brownian motion and particle heterogeneity). Upon studying the relationship between O_R and O_P (Figure 4B), their negative correlation indicates that the collective structure remains either the rotating state or the polar state (rather than the swarm state) in most of the time, implying that the group can maintain the ordered movement under perturbations. The high correlation between O_R and O_P can always be observed at relatively high particle density but disappears in the low-density

region (Figure S14), which proves that the group remains in the disordered state in the low-density region due to a lesser probability of information exchange among particles.

To quantitatively understand the robustness of the group, two ordered collective states (i.e., rotating and polar states) along with the disordered swarm state and transition state are first defined according to the values of $|O_R|$ and O_P (Methods). We then visualize the fraction of time spent in four states at $\rho = 0.214$ during experiments and three different simulation conditions (no noise, with Brownian motion, with Brownian motion and heterogeneity), respectively (Figure 4C). Overall, both simulations and experiments indicate that the collective structure spends most of the time in the rotating state while spending little time visiting the polar or swarm states, which could be attributed to the circular shape of the confined geometry (Movies S1 and S11) and the persistent cohesion of the group. Besides, mainly because the heterogeneity of the active particles used in our experiment is relatively small (Figure S5), only Brownian motion will significantly reduce the probability of the rotating states while the particle heterogeneity contributes less here. The small gap between the experiments and simulations can be ascribed to other experimental factors such as the hydrodynamic interaction, substrate roughness, and system uncertainty of particle manipulation that are not included in our simulations.

We further analyzed the state-switching frequency, i.e., the number of state switches per unit time, and the probability that the structure can return to the preceding ordered states (Figure 4D). Although the rotation state is quite stable among particles without any perturbations, state switching occurs occasionally due to the settings of the virtual boundary condition and long-range physical interaction (Methods and Movie S9). As for the influence of different perturbations, both Brownian motion and particle heterogeneity can increase the state-switching frequency while Brownian motion has a more pronounced influence in our current case (Figure 4C and 4D). Intriguingly, with the existence of perturbations, the probability of the structure maintaining the preceding ordered states can still exceed 60% (the blue line in Figure 4D), proving the high robustness of the collective structure.

Finally, we exploit our experimental setup to study several influential variants of the conventional Vicsek model. Unlike the above interactions determined by the metric distance, the particles can also achieve velocity alignment using their topological distance which has already been theoretically analyzed[24] and found in starling flocks.[3] Here, we define the topological distance to be the seven closest neighbors around each particle (Figure 5A) as its interacting counterparts, while all the other experimental settings remain the same. Due to the persistent information exchange ensured by the topological interaction, the collective structure can become highly polar and coherent even at extremely low particle density (Figure 5B and Movie S10). Compared to the metric interaction, the collective motion has higher $\langle O_P \rangle$ than $\langle |O_R| \rangle$ and no critical density is observed in the same density range (Figure 5C). A more comprehensive discussion on the topological interaction will be given in our future work. Furthermore, since the reflective boundary condition is defined by the algorithm, we can change it to arbitrary shapes to probe how the geometry's shape influences the collective motion. For instance, a square-confined geometry results in a new trapping state (i.e., particles jam at the corner) along with rotating and polar states (Figure 5D and Movie S11). Also, particles in an off-center ring-shaped geometry can be trapped

occasionally at the neck of the ring while bidirectional rotation is observed as well (Figure 5E and Movie S12). By adding more boundaries within the circle, the current setup can also be used to investigate the influence of multiple obstacles on collective motion.

5. Discussion

we have successfully developed a new optical feedback-control platform that enables synchronous control of arbitrarily navigated active particles for investigating collective motion through velocity alignment. Compared to existing focused-light-powered active-particle platforms,[18–23] our experimental platform represents a significant advancement. Notably, we have recently developed a new manipulation technique that enhances the reorientation capability of particles.[26] This new technique, coupled with the synchronous control of multiple particles facilitated by the SLM, enables a higher degree of customization and the study of a wider range of models. Though the existing platform can also lead to several similar observations such as vortex formation and state transition[21a, 22] reported here (which is common as similar collective motions can stem from different models[1]), their applied models can only be those that are insensitive to the reorientation capability of individuals. Herein, we explore a different and more generic model (i.e., the Vicsek model), to investigate its effectiveness in real perturbed environments, which was quite challenging to realize previously. In addition, we have observed ordered movements and special density-dependent state transitions through the synergy of information exchange and the long-range physical interaction. Furthermore, we have demonstrated that Brownian motion and particle heterogeneity increase the frequency of state switching while having limited influence on the robustness of the structure. It is worth noting that, under the current condition of our platform, the upper limit for the number of controlled particles is expected to reach 100–200 particles (Supplementary Note 2.3), which is generally sufficient to replicate the collective motion of major natural systems such as fishes,[34] birds,[35] sheep,[36] locusts,[9] and ants.[37]

Moreover, our method serves as an essential bridge between direct observation and analysis of collective living objects and purely theoretical modeling of collective motion. It provides a means to explore collective motion in the real world with known and controllable experimental inputs. Specifically, we can further enhance our experimental platform by modifying our control program to incorporate additional factors that have been identified to influence collective motion in living species. These factors can include time delay,[38] hierarchy,[39] leadership,[11d] and vision cone,[40] etc., all of which can be mathematically defined using the position and velocity information of the agents. Since our platform already provides the relevant information by real-time imaging analysis, incorporating these additional factors is as simple as substituting or modifying the equations in the “Velocity Alignment” section described in Methods. For example, we can introduce time delay by changing the equation $\theta_j^{t+\Delta t_0} = \arg\left[\sum_{k \in C_j}(\exp i\theta_{k,\mathrm{real}}^{t})\right]$ to $\theta_j^{t+\Delta t_0} = \arg\left[\sum_{k \in C_j}(\exp i\theta_{k,\mathrm{real}}^{t-\tau})\right]$. We can further control our sample substrates to account for complex environmental factors like flows and physical boundaries. For example, microfluidic systems can be integrated onto the substrates to introduce external flows to the active particles, simulating the living conditions of aquatic animals. Microfabrication techniques such as photolithography can be

employed to create diverse microstructures on our substrates to act as physical boundaries of the active particles. This enhanced platform will empower us to conduct in-depth parametric and quantitative analyses, revealing the influence of different factor combinations on collective motion. Through this capability, we can gain a profound understanding of the individual roles of these factors as well as their synergistic effects, leading to a thorough comprehension of their impact. Additionally, by integrating automation with the motorized stage, our platform enables the implementation of collective motion in free space for fundamental studies and the development of intelligent swarm microrobotics. In summary, our novel optical feedback-control platform opens up new avenues for studying collective motion, expanding the understanding of active-particle systems, and advancing the field of swarm microrobotics.

6. Experimental Section/Methods

Sample preparation:

Our sample was prepared according to Ref. [29] and [26]. Overall, a solution consisting of polyethylene glycol (PEG), phosphate-buffered saline (PBS), and silica microspheres were added on a Bovine-Serum-Albumin (BSA)-coated thermoplasmonic substrate confined by a spacer and then covered by an upper coverslip. The concentration of PBS (Sigma-Aldrich, 806552) and PEG (Sigma-Aldrich, 8.18897) was prepared in 5 wt %. The silica microspheres with a mean diameter being 1.97 μm (Bangs Laboratories, SS04002) were diluted in the PEG/PBS solution by 400 times. The solvent was deionized water (Milli-Q). The thermoplasmonic substrate composed of randomly distributed gold nanoparticles was fabricated in two steps: First, 5.5-nm gold film was deposited on glass slides by physical vapor deposition (Kurt J. Lesker, PVD 75) at a base pressure of 1×10^{-5} Torr with the deposition rate being 0.5 Å s^{-1}. Then, the gold film was annealed at 550 °C for 2 h. For the surface coating of BSA, the thermoplasmonic substrate was further immersed in 1 wt % BSA (Sigma-Aldrich, A8531) at room temperature for 24 h, followed by rinsing with deionized water and drying under a nitrogen stream.

Hardware:

A schematic of the experimental devices and the information flow is shown in Figure S1. A 660 nm laser beam (Laser Quantum, Opus 660) was first expanded with a 5× beam expander (Thorlabs, GBE05-A). Then, it was reflected by a liquid crystal on silicon-spatial light modulator (LCOS-SLM, Hamamatsu, X13138-01, resolution: 1392×1040 pixels) and propagated along a 4f optical system with $f_1 = 0.75$ m and $f_2 = 1$ m. Finally, it was directed into an inverted optical microscope (Nikon, Ti2) with a 60× oil objective (Nikon, CFI Plan Fluor 60XS Oil) for the optical-induced nudging of particles. a charge-coupled device camera (Lumenera, INFINITY 2) was used to acquire the optical images. A Notch filter (658 nm) was placed between the objective and the camera to block the incident laser beam for the camera. The real-time image was transferred to a computer with the Intel Core i7 center processing unit and AMD Radeon HD 8570 graphic card.

Software and algorithm:

All programs for automated feedback control were homebuilt based on LabVIEW (Version 2019 SP1, National Instruments). The main elements of the program are shown in Figure S1B:

Raw-image input:

The color image was first acquired by the default Vision Acquisition module in LabVIEW and then transformed into a binary one with a preset threshold, by which each particle had an isolated and stable white center while the background noise was minimized.

Particle filtering:

Particle filtering includes two steps: first, use the area threshold to differentiate particles from the background noise; second, exclude particles outside the confined geometries based on the distance between the particle center and the confined geometry center. Note that different geometries, such as circle versus square, will need to modify this criterion.

Particle labeling:

This is challenging because all the particles in the image are almost identical, but the non-physical interaction rule requires us to differentiate them and let them have their own histories of positions and velocities. Since the particle here would only move the distance equal to ~10 % of its diameter at most between two image frames, thus, we first got the position differences among all particles between every two neighboring image frames, and then used a distance threshold (here to be half of the particle diameter) to differentiate them, below which certain particle of the current frame was recognized as the corresponding particle from the previous frame.

Velocity calculation:

After labeling the particles, the real-time velocity of each particle could be calculated directly based on its temporal positions. Meanwhile, we also integrated the calculation of O_R and O_P into the program, whose values versus time could be checked during the experiment or exported after finishing the experiment.

Velocity Alignment:

The neighbors of each particle were recognized whenever the metric distance between two particles was smaller than the preset interacting radius r_0 (Note that for topological distance in this work, the neighbors were defined by the nearest seven particles). Then, the new direction for the next execution was calculated based on $\theta_j^{t+\Delta t_0} = \arg\left[\sum_{k \in C_j} (\exp i\theta_{k,\mathrm{real}}^t)\right]$,[24] where $\theta_{k,\mathrm{real}}^t$ is the real moving angle of particle k at time t that was provided by the previous Velocity calculation module.

Volume exclusion:

If the particle has at least one neighboring particle within its volume exclusion region, its new direction will be determined by the volume exclusion equation:

$\theta_j^{t+\Delta t_0} = -\arg\left(\sum_{k\in C_j^{ve}}^{k\neq j} \frac{\boldsymbol{r}_{jk}^t}{|\boldsymbol{r}_{jk}^t|}\right)$ with C_j^{ve} being the repelling zone (defined by radius r_{ve}) of the particle j and $\boldsymbol{r}_{jk}^t$ being the unit vector in the direction from the particle j to its neighbor k.[11a]

Boundary reflection:

Herein, all the boundary conditions were virtually defined. This could help to quickly investigate different sizes and shapes of various boundary conditions as well as get ready for future study on soft boundaries,[28] whose size and shape are dynamically tuned according to the spatial distribution of particles, such as what occurs within cell membranes. The particle was determined to hit the boundary by measuring the distance between the particle center and the geometry center (r_{j-b}^t). Due to the discrete image capture, the particles could hit the boundary between two image frames. Thus, we must introduce an 'interacting thickness' (Δr_b) to the boundary condition. Whenever $r_{j-b}^t \in [r_b,\ r_b + \Delta r_b]$, the particle's movement would be regulated by the boundary reflection. The new direction was determined by $\boldsymbol{n}_j^{t+\Delta t_0} = \boldsymbol{n}_j^t - 2(\boldsymbol{n}_j^t \cdot \boldsymbol{n}_{j-b}^t)\boldsymbol{n}_{j-b}^t$ with $\boldsymbol{n}_j^t = (\cos\theta_j^t, \sin\theta_j^t)$ and $\boldsymbol{n}_{j-b}^t$ being the normal vector of $\boldsymbol{r}_{j-b}^t$.[25] Δr_b is set as 0.39 μm according to $\Delta r_b = 2 \times v_{tot,max} \times \Delta t_0$ to ensure that the boundary reflection always takes effect.

We also observed that the particles could sometimes exceed $r_b + \Delta r_b$, which was not due to the malfunction of the control program but because the long-range physical repulsion forces from their neighboring particles could sometimes be too high to push the particles out of the boundary. Since this was attributed to the high extra repulsion forces in the direction normal to the boundary, we let $\boldsymbol{n}_j^{t+\Delta t_0} = -\boldsymbol{n}_{j-b}^t$ when $r_{j-b}^t > r_b + \Delta r_b$. This additional change of particle directions could lead to occasional state switches of the collective structure even without any perturbations (Movie S9). Note that once the particle was judged hitting the boundary, its direction was priorly determined by the boundary rather than volume exclusion or velocity alignment. Besides, if a real physical boundary condition is required, physical microstructures could be added to our substrates by microfabrication such as photolithography.

Laser spot calculation:

The laser for each particle was placed 0.93 μm away from the particle center (i.e., at the circumference of the particle), and its exact position was determined by the calculated moving direction of each particle.

Hologram output:

The spatial information of the lasers was then transformed into holograms and transferred to the spatial light modulator to diffract the single laser input into the desired laser patterns. This part was implemented based on the "Red tweezers" developed by R. Bowman et al.[41]

It's worth noting that the system time delay due to the imaging capture, processing and hologram generation is ~ 132 ms. This system time delay will make each particle have larger angle deviation than the ideal case without any system time delay. But by using the method

in ref. [33], we have already quantified the motion of particles (Supplementary Note 1.1) under the consideration of the influence of the system time delay.

Analysis of experimental data:

The experimental videos were processed by our homebuilt MATLAB program (R2021b). Each image frame was first cropped according to the size of the boundary and then transferred into a binary image. Next, all the connected white pixels were grouped and could be regarded as the center of certain particles once their area exceeded a predefined threshold. Then, all the particles were differentiated and labeled according to the above *particle labeling* section. Finally, the particle velocities, O_R and O_P versus time were calculated and exported. The $\langle|O_R|\rangle$ and $\langle O_P\rangle$ of one experimental video was calculated by averaging its second half of $|O_R|$ and O_P versus time curves, and the $\langle|O_R|\rangle$ and $\langle O_P\rangle$ at certain density was obtained by averaging $\langle|O_R|\rangle$ and $\langle O_P\rangle$ of different videos.

Definition of four collective states:

To quantitatively understand the state-transition behaviors, four collective states including rotation, polarization, swarm, and transition were defined by setting the thresholds for $|O_R|$ and O_P. As mentioned in ref. [8a], there is never a general standard for the state definitions and we could only use a heuristic approach to estimate the thresholds of $|O_R|$ and O_P based on the $O_R - O_P$ histogram and visual verification from the experimental videos. Therefore, the states were defined as the rotating state ($|O_R| > 0.45$ and $O_P < 0.25$), the polar state ($|O_R| < 0.25$ and $O_P > 0.45$) the swarm state ($|O_R| < 0.25$ and $O_P < 0.25$) and the transition state ($|O_R|$ and O_P are out of all the above regions) based on the experimental videos and O_R/O_P values versus time.

Calculation on the time portion of different states and the state-switching frequencies:

We used the data of $|O_R|$ and O_P versus time in steady state (i.e., the second half of each dataset) to calculate the time portion of four states and the state-switching frequency. All the data were first smoothed by using an average with a span of 20-time steps (corresponding to 2.64 seconds). Then, different states were defined based on the discussion above. The states that lasted less than 10 timesteps (i.e., ~1.32 s) would be regarded as fluctuations and not be counted. Finally, the time portions and switch frequencies of different states under different experimental realizations and simulation conditions were obtained.

Modeling and Simulations:

The simulations were performed in MATLAB (R2021b) in consideration of the information exchange (including velocity alignment, volume exclusion, and boundary reflection), long-range physical interaction, Brownian motion, and particle heterogeneity (Figure S4). Each simulation data point in the main text is averaged over 20 realizations that have different initial states. Single realization will run 8,000 timesteps and only the last 4,000 data points will be averaged to represent the value for this realization, which ensure that all the values are obtained at the steady state of the collective motion. The 20 realizations and 8,000 timesteps are determined by the convergence test (Figure S7). Primarily, the position of each particle is determined by

$$\boldsymbol{r}_j^{t+\Delta t_0} = \boldsymbol{r}_j^t + \boldsymbol{v}_j^t \, \Delta \, t_0 \tag{4}$$

with $\boldsymbol{v}_j^t$ being the real-time velocity in consideration of laser propulsion, neighboring-particle-laser effect, Brownian motion, and particle heterogeneity. Then, we can decouple $\boldsymbol{v}_j^t$ by $\boldsymbol{v}_j^t = \boldsymbol{v}_{j,\parallel}^t + \boldsymbol{v}_{j,\perp}^t$ and the following Langevin equation:

$$\boldsymbol{v}_{j,\parallel}^t = \boldsymbol{v}_{j,\,\mathrm{tot}}^t \cos\delta + \sqrt{2D_j}\xi_\parallel^t \tag{5}$$

$$\boldsymbol{v}_{j,\perp}^t = \boldsymbol{v}_{j,\,\mathrm{tot}}^t \sin\delta + \sqrt{2D_j}\xi_\perp^t \tag{6}$$

where $\boldsymbol{v}_{j,\,\mathrm{tot}}^t$ is the velocity determined by the sum of all the laser influences (including the laser always at the particle's circumference and the neighboring lasers following the neighboring particles), D_j is the diffusion coefficient which varies among different particles due to the heterogeneity of particle sizes and surface charges (Figure S5); $\xi_\parallel^t$ and $\xi_\perp^t$ are zero-mean, unit-variance independent Gaussian white noises from the Brownian motion.

Furthermore, $\boldsymbol{v}_{j,\mathrm{tot}}^t$ are determined by

$$\boldsymbol{v}_{j,\mathrm{tot}}^t = \boldsymbol{v}_{j,\mathrm{laser}} + \sum \boldsymbol{v}_{\mathrm{k-j,\,laser}}^t(d_{\mathrm{k-j}}^t) \tag{7}$$

where $\boldsymbol{v}_{j,\mathrm{laser}}$ comes from the laser at the particle's circumference, whose direction is determined by θ_j^t but whose magnitude varies among the different particles (Figure 2C); $\boldsymbol{v}_{\mathrm{k-j,\,laser}}^t(d_{\mathrm{k-j}}^t)$ is the extra velocity induced by the laser beams from the neighboring particle k, whose magnitude and direction ($\phi_{\mathrm{k-j,\,laser}}^t$) are determined by

$$d_{\mathrm{k-j}}^t = \sqrt{R^2 + \left(d_{\mathrm{k-j,\,center}}^t\right)^2 - 2Rd_{\mathrm{k-j,\,center}}^t \cos(\theta_j^t - \theta_k^t)} \tag{8}$$

$$v_{\mathrm{k-j,\,laser}}^t = \frac{C_2 d_{\mathrm{k-j}}^t}{\left(d_{\mathrm{k-j}}^t\right)^2 + R^2} \frac{v_{j,\mathrm{laser}}}{v_{\mathrm{avg,\,laser}}} \tag{9}$$

$$\phi_{\mathrm{k-j,\,laser}}^t = \theta_j^t + \mathrm{asin}\left(\frac{R}{d_{\mathrm{k-j}}^t} \sin(\theta_j^t - \theta_k^t)\right)$$

(10)

where d^t_{k-j} is the distance between the geometric center of particle j and the laser position that follows particle k; R is the particle radius; $d^t_{k-j,\text{center}}$ is the distance from the particle center j to particle center k. In addition, since $v_{\text{avg, laser}}$ is the measured average velocity among different particles, thus $\frac{v_{j,\text{laser}}}{v_{\text{avg,laser}}}$ is the normalization coefficient that modifies the laser influence on particle j under the consideration of particle heterogeneity. For the constants used in the simulations, their values are: $\Delta t_0 \approx 0.132$ s (mainly determined by the frame rate of the camera), $\delta = N(0,\ 0.24^2)$ (Supplementary Note 1.2), $D_j = N\left(0.018,\ 0.0025^2\right)$ μm^2 s^{-1} (Figure S5), $\xi^t_{\parallel} = \xi^t_{\perp} = N(0,1)$, $\boldsymbol{v}_{j,\text{laser}} = N\left(1.34,\ 0.08^2\right)$ μm s^{-1} (Figure 2D), $R = 0.985$ μm and $v_{\text{laser}} = 1.34$ μm s^{-1}.

Statistical Analysis:

All the data with error bars are presented as mean ± SD. The sample sizes of experimental and simulated data are $n \geq 5$ and $n = 20$, respectively.

Supplementary Material

Refer to Web version on PubMed Central for supplementary material.

Acknowledgements

We thank Dr. Kan Yao and Dr. Richard Bowman for stimulating discussions. All authors acknowledge financial support from the National Science Foundation (NSF-ECCS-2001650) and the National Institute of General Medical Sciences of the National Institutes of Health (R01GM146962).

References

[1]. Vicsek T, Zafeiris A, Phys. Rep 2012, 517, 71.

[2]. a)Parrish JK, Viscido SV, Grünbaum D, The Biol. Bull 2002, 202, 296; [PubMed: 12087003] b)Berdahl A, Torney CJ, Ioannou CC, Faria JJ, Couzin ID, Science 2013, 339, 574. [PubMed: 23372013]

[3]. Ballerini M, Cabibbo N, Candelier R, Cavagna A, Cisbani E, Giardina I, Lecomte V, Orlandi A, Parisi G, Procaccini A, Viale M, Zdravkovic V, Proc. Natl. Acad. Sci. 2008, 105, 1232. [PubMed: 18227508]

[4]. a)Zhang HP, Be'er A, Florin E-L, Swinney HL, Proc. Natl. Acad. Sci. 2010, 107, 13626; [PubMed: 20643957] b)Chen C, Liu S, Shi X.-q., Chaté H, Wu Y, Nature 2017, 542, 210. [PubMed: 28114301]

[5]. Wu K-T, Hishamunda JB, Chen DTN, DeCamp SJ, Chang Y-W, Fernández-Nieves A, Fraden S, Dogic Z, Science 2017, 355, eaal1979. [PubMed: 28336609]

[6]. Attanasi A, Cavagna A, Del Castello L, Giardina I, Melillo S, Parisi L, Pohl O, Rossaro B, Shen E, Silvestri E, Viale M, PLOS Comput. Biol. 2014, 10, e1003697. [PubMed: 25057853]

[7]. Bialek W, Cavagna A, Giardina I, Mora T, Silvestri E, Viale M, Walczak AM, Proc. Natl. Acad. Sci. 2012, 109, 4786. [PubMed: 22427355]

[8]. a)Tunstrøm K, Katz Y, Ioannou CC, Huepe C, Lutz MJ, Couzin ID, PLOS Comput. Biol. 2013, 9, e1002915; [PubMed: 23468605] b)Sumino Y, Nagai KH, Shitaka Y, Tanaka D, Yoshikawa K, Chaté H, Oiwa K, Nature 2012, 483, 448; [PubMed: 22437613] c)Hamby AE, Vig DK, Safonova S, Wolgemuth CW, Sci. Adv. 2018, 4, eaau0125; [PubMed: 30585288] d)Wioland H, Woodhouse FG, Dunkel J, Kessler JO, Goldstein RE, Phys. Rev. Lett. 2013, 110, 268102;

[PubMed: 23848925] e)Schaller V, Weber C, Semmrich C, Frey E, Bausch AR, Nature 2010, 467, 73. [PubMed: 20811454]

[9]. Buhl J, Sumpter DJT, Couzin ID, Hale JJ, Despland E, Miller ER, Simpson SJ, Science 2006, 312, 1402. [PubMed: 16741126]

[10]. a)Cavagna A, Conti D, Creato C, Del Castello L, Giardina I, Grigera TS, Melillo S, Parisi L, Viale M, Nat. Phys. 2017, 13, 914;b)Attanasi A, Cavagna A, Del Castello L, Giardina I, Grigera TS, Jelić A, Melillo S, Parisi L, Pohl O, Shen E, Viale M, Nat. Phys. 2014, 10, 691;c)Silverberg JL, Bierbaum M, Sethna JP, Cohen I, Phys. Rev. Lett. 2013, 110, 228701; [PubMed: 23767754] d)Moussaïd M, Helbing D, Theraulaz G, Proc. Natl. Acad. Sci. 2011, 108, 6884; [PubMed: 21502518] e)Lukeman R, Li Y-X, Edelstein-Keshet L, Proc. Natl. Acad. Sci. 2010, 107, 12576; [PubMed: 20616032] f)Cavagna A, Cimarelli A, Giardina I, Parisi G, Santagati R, Stefanini F, Viale M, Proc. Natl. Acad. Sci. 2010, 107, 11865; [PubMed: 20547832] g)Schneidman E, Berry MJ, Segev R, Bialek W, Nature 2006, 440, 1007; [PubMed: 16625187] h)Czirók A, Ben-Jacob E, Cohen I, Vicsek T, Phys. Rev. E 1996, 54, 1791.

[11]. a)Couzin ID, Krause J, James R, Ruxton GD, Franks NR, J. Theor. Biol. 2002, 218, 1; [PubMed: 12297066] b)Cucker F, Smale S, IEEE Trans. Autom. Control 2007, 52, 852;c)Vicsek T, Czirók A, Ben-Jacob E, Cohen I, Shochet O, Phys. Rev. Lett. 1995, 75, 1226; [PubMed: 10060237] d)Couzin ID, Krause J, Franks NR, Levin SA, Nature 2005, 433, 513; [PubMed: 15690039] e)Bastien R, Romanczuk P, Sci. Adv 2020, 6, eaay0792. [PubMed: 32076645]

[12]. a)Vásárhelyi G, Virágh C, Somorjai G, Nepusz T, Eiben AE, Vicsek T, Sci. Robot. 2018, 3, eaat3536; [PubMed: 33141727] b)Mijalkov M, McDaniel A, Wehr J, Volpe G, Phys. Rev. X 2016, 6, 011008;c)Chvykov P, Berrueta TA, Vardhan A, Savoie W, Samland A, Murphey TD, Wiesenfeld K, Goldman DI, England JL, Science 2021, 371, 90. [PubMed: 33384378]

[13]. a)Bechinger C, Di Leonardo R, Löwen H, Reichhardt C, Volpe G, Volpe G, Rev. Mod. Phys. 2016, 88, 045006;b)Shaebani MR, Wysocki A, Winkler RG, Gompper G, Rieger H, Nat. Rev. Phys. 2020, 2, 181.

[14]. a)Driscoll M, Delmotte B, Youssef M, Sacanna S, Donev A, Chaikin P, Nat. Phys. 2017, 13, 375;b)Kokot G, Snezhko A, Nat. Commun. 2018, 9, 2344; [PubMed: 29904114] c)Wang W, Gardi G, Malgaretti P, Kishore V, Koens L, Son D, Gilbert H, Wu Z, Harwani P, Lauga E, Holm C, Sitti M, Sci. Adv. 2022, 8, eabk0685; [PubMed: 35030013] d)Xie H, Sun M, Fan X, Lin Z, Chen W, Wang L, Dong L, He Q, Sci. Robot. 2019, 4;e)Han K, Kokot G, Tovkach O, Glatz A, Aranson IS, Snezhko A, Proc. Natl. Acad. Sci. 2020, 117, 9706. [PubMed: 32300010]

[15]. a)Bricard A, Caussin J-B, Desreumaux N, Dauchot O, Bartolo D, Nature 2013, 503, 95; [PubMed: 24201282] b)Yan J, Han M, Zhang J, Xu C, Luijten E, Granick S, Nat. Mater. 2016, 15, 1095; [PubMed: 27400388] c)Zhang J, Alert R, Yan J, Wingreen NS, Granick S, Nat. Phys. 2021, 17, 961;d)Shen Y, Dierking I, Nat. Commun. 2022, 13, 2122. [PubMed: 35440645]

[16]. a)Theurkauff I, Cottin-Bizonne C, Palacci J, Ybert C, Bocquet L, Phys. Rev. Lett. 2012, 108, 268303; [PubMed: 23005020] b)Ginot F, Theurkauff I, Detcheverry F, Ybert C, Cottin-Bizonne C, Nat. Commun. 2018, 9, 696. [PubMed: 29449564]

[17]. Palacci J, Sacanna S, Steinberg AP, Pine DJ, Chaikin PM, Science 2013, 339, 936. [PubMed: 23371555]

[18]. Khadka U, Holubec V, Yang H, Cichos F, Nat. Commun. 2018, 9, 3864. [PubMed: 30242284]

[19]. Bäuerle T, Fischer A, Speck T, Bechinger C, Nat. Commun. 2018, 9, 3232. [PubMed: 30104679]

[20]. Lavergne FA, Wendehenne H, Bäuerle T, Bechinger C, Science 2019, 364, 70. [PubMed: 30948548]

[21]. a)Bäuerle T, Löffler RC, Bechinger C, Nat. Commun. 2020, 11, 2547; [PubMed: 32439919] b)Wang X, Chen P-C, Kroy K, Holubec V, Cichos F, Nat. Commun. 2023, 14, 56. [PubMed: 36599830]

[22]. Löffler RC, Bäuerle T, Kardar M, Rohwer CM, Bechinger C, Europhys. Lett. 2021, 134, 64001.

[23]. Chen C-J, Bechinger C, New J Phys. 2022, 24, 033001.

[24]. Ginelli F, Chaté H, Phys. Rev. Lett. 2010, 105, 168103. [PubMed: 21231019]

[25]. Armbruster D, Motsch S, Thatcher A, Phys. D: Nonlinear Phenom 2017, 344, 58.

[26]. Ding H, Chen Z, Kollipara PS, Liu Y, Kim Y, Huang S, Zheng Y, ACS Nano 2022, 16, 10878. [PubMed: 35816157]

[27]. Volpe G, Gigan S, Volpe G, Am. J. Phys. 2014, 82, 659.

[28]. Araújo NA, Janssen L, Barois T, Boffetta G, Cohen I, Corbetta A, Dauchot O, Dijkstra M, Durham WM, Dussutour A, Soft Matter 2023, 19, 1695. [PubMed: 36779972]

[29]. Ding H, Kollipara PS, Kim Y, Kotnala A, Li J, Chen Z, Zheng Y, Sci. Adv. 2022, 8, eabn8498. [PubMed: 35704582]

[30]. Filella A, Nadal F, Sire C, Kanso E, Eloy C, Phys. Rev. Lett. 2018, 120, 198101. [PubMed: 29799263]

[31]. Jolles JW, King AJ, Killen SS, Trends Ecol. Evol. 2020, 35, 278. [PubMed: 31879039]

[32]. a)Patra P, Beyer K, Jaiswal A, Battista A, Rohr K, Frischknecht F, Schwarz US, Nat. Phys. 2022, 18, 586;b)Mattingly HH, Emonet T, Proc. Natl. Acad. Sci. 2022, 119, e2117377119. [PubMed: 35727978]

[33]. Fränzl M, Muiños-Landin S, Holubec V, Cichos F, ACS Nano 2021, 15, 3434. [PubMed: 33556235]

[34]. Jhawar J, Morris RG, Amith-Kumar UR, Danny Raj M, Rogers T, Rajendran H, Guttal V, Nat. Phys. 2020, 16, 488.

[35]. Flack A, Nagy M, Fiedler W, Couzin ID, Wikelski M, Science 2018, 360, 911. [PubMed: 29798883]

[36]. Gómez-Nava L, Bon R, Peruani F, Nat. Phys. 2022, 18, 1494.

[37]. Anderson C, Fernandez-Nieves A, Nat. Commun. 2022, 13, 6710. [PubMed: 36344501]

[38]. a)Holubec V, Geiss D, Loos SAM, Kroy K, Cichos F, Phys. Rev. Lett. 2021, 127, 258001; [PubMed: 35029446] b)Zhang HT, Chen MZ, Stan GB, Zhou T, Maciejowski JM, IEEE Circuits Syst. Mag. 2008, 8, 67.

[39]. Nagy M, Ákos Z, Biro D, Vicsek T, Nature 2010, 464, 890. [PubMed: 20376149]

[40]. Durve M, Saha A, Sayeed A, Eur. Phys. J. E 2018, 41, 49. [PubMed: 29626264]

[41]. Bowman RW, Gibson GM, Linnenberger A, Phillips DB, Grieve JA, Carberry DM, Serati S, Miles MJ, Padgett MJ, Comput. Phys. Commun. 2014, 185, 268.

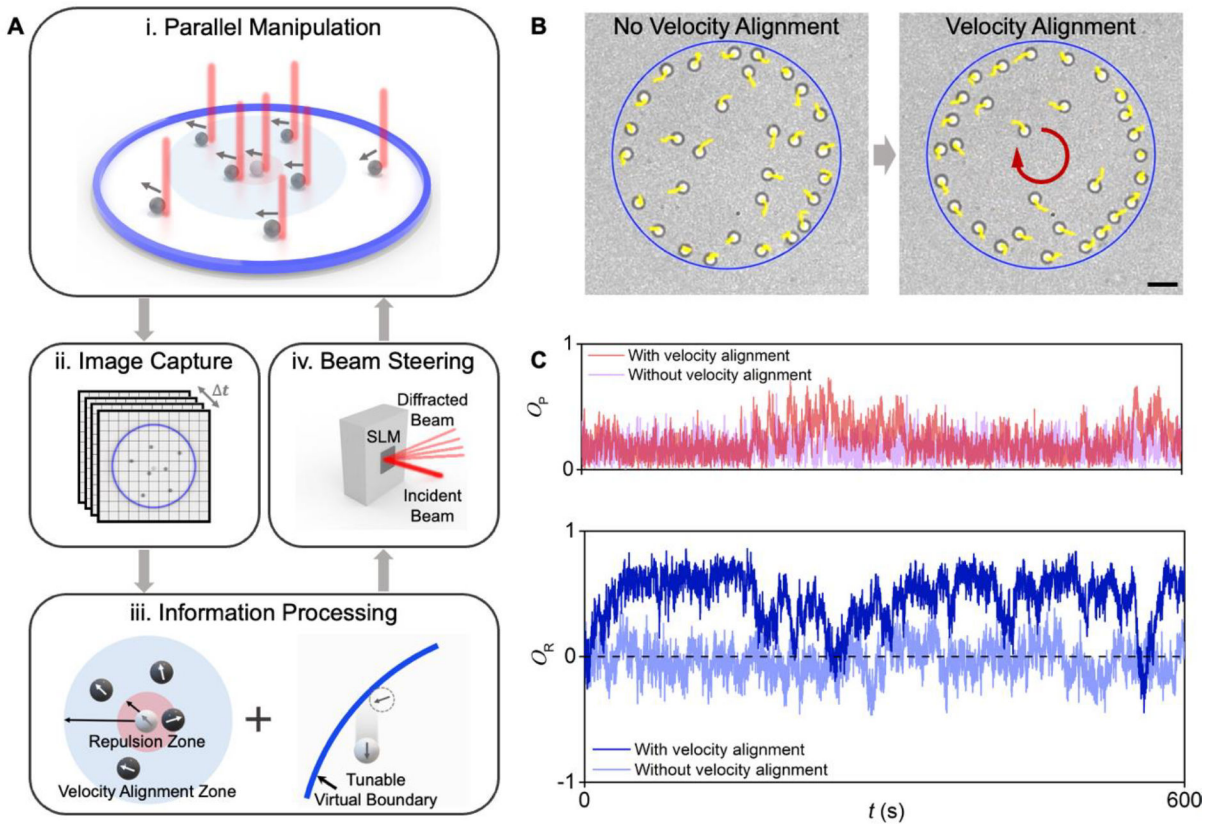

Figure 1. Experimental realization of collection motion within a confined geometry based on velocity alignment.

(A) Schematic of the feedback control experimental setup. A computer is connected to a camera and a SLM. Real-time images from the camera are transferred to the computer for the information processing. Then, the calculated holographic data are transferred to the SLM to update the spatial laser pattern. (B) Optical images of active particles overlayed with their trajectories (yellow line) and their boundary (blue circle) without velocity alignment (left) and with velocity alignment (right). The red arrow in the middle of the image indicates the rotation direction of the collective structure. Scale bar: 5 μm. (C) Time-varied rotation (blue, bottom panel) and polarization (red, top panel) order parameters of the experimental realization corresponding to (B).

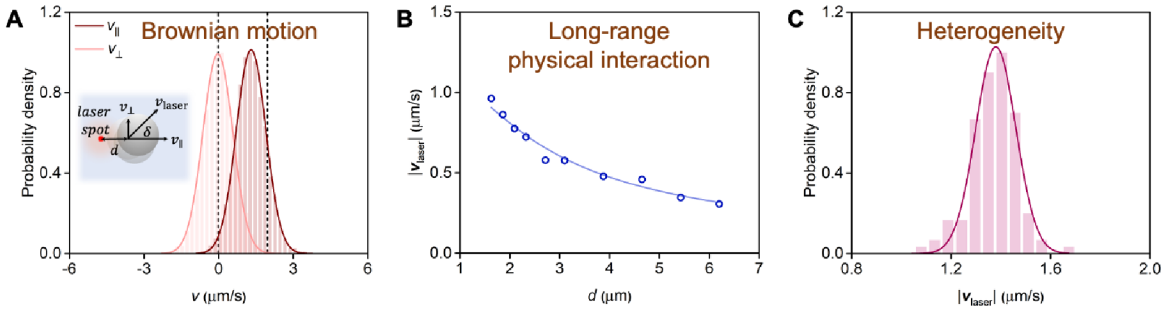

Figure 2. Velocity characterization for Brownian motion, laser-particle-distance dependence, and heterogeneity.

(A) The probability density distribution of $v_\parallel$ and $v_\perp$ fitted by the normal distribution function. The inset shows the schematic of single particle driven by the laser-induced localized thermal field with the propulsion velocity ($\boldsymbol{v}_{laser}$). d represents the laser-particle distance. The direction deviation (δ) compared to the supposed moving direction ($\frac{\boldsymbol{v}_\parallel}{|\boldsymbol{v}_\parallel|}$) is due to the Brownian motion and the unavoidable experimental feedback delay. Note that $\boldsymbol{v}_{laser}$ is not directly composed of $\boldsymbol{v}_\parallel$ and $\boldsymbol{v}_\perp$ (See Supplementary Note 1.1). (B) The plot of $|\boldsymbol{v}_{laser}|$ versus d. The hollow dots represent experimental values while the blue curve is corresponding to the equation S6 shown in the supplementary note 1.2. (C) The probability density distribution of $|\boldsymbol{v}_{tot}|$ of 120 different particles and fitted by the normal distribution. The measurement in (A) and (C) is performed under d = 0.93 μm.

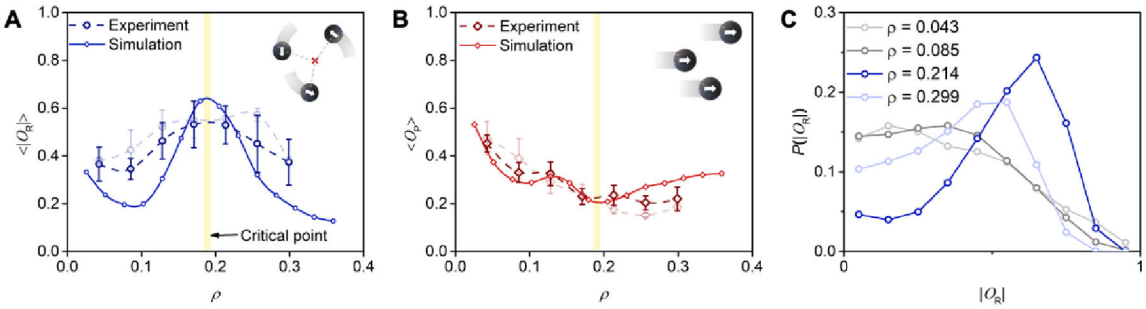

Figure 3. Measuring, modeling, and active tuning of collective motion.

Plots of (A) $\langle |O_R| \rangle$ and (B) $\langle O_P \rangle$ versus particle density for the experimental measurements (dashed lines) and simulation results (solid lines). The dark dashed lines represent the results where the real-time particle velocities in experiments are calculated based on the two nearest image frames (i.e., $\Delta t = \Delta t_0 \approx 0.132$ s), while the shallow dashed lines indicate the results where particle velocities are calculated based on the average over eight image frames (i.e., $\Delta t = 8\,\Delta t_0 \approx 1.06$ s). The simulation results include the effects of Brownian motion and particle heterogeneity. (C) The probability distribution of experimental $|O_R|$ under different particle densities. The sample sizes of experimental and simulated data are $n \geq 5$ and $n = 20$, respectively. The error bars indicate the standard deviation.

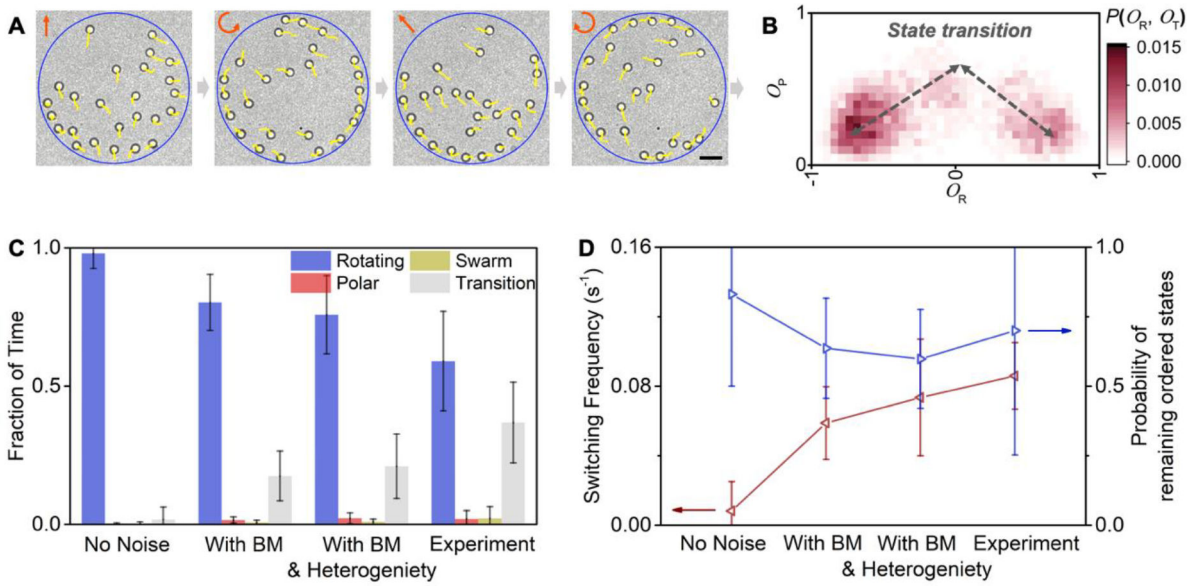

Figure 4. Statistics of the state transition around the critical density (Yellow region in Figure 3a and 3b).

(A) Sequential optical images of the collective motion at $\rho = 0.214$. The blue circle and yellow traces represent the boundary and the particle trajectories within the last six seconds, respectively. The red symbols at the top right corner indicate the motion directions of the group. Scale bar: 5 μm. (B) Histogram of the correlation between O_R and O_P. (C) Fraction of time spent in different states for three simulation conditions (no noise / with Brownian motion (BM) / with BM & heterogeneity) and the experiment at $\rho = 0.214$. (D) The plot of the switching frequency among four states (the red line) and their corresponding portion remaining in the same ordered states (the blue line). Remaining in the same ordered states means two conditions: from the rotating to transition then back to the rotating state and from the polar to transition then back to the polar state. The sample sizes of experimental and simulated data are $n \geq 5$ and $n = 20$, respectively. All the error bars indicate the standard deviation.

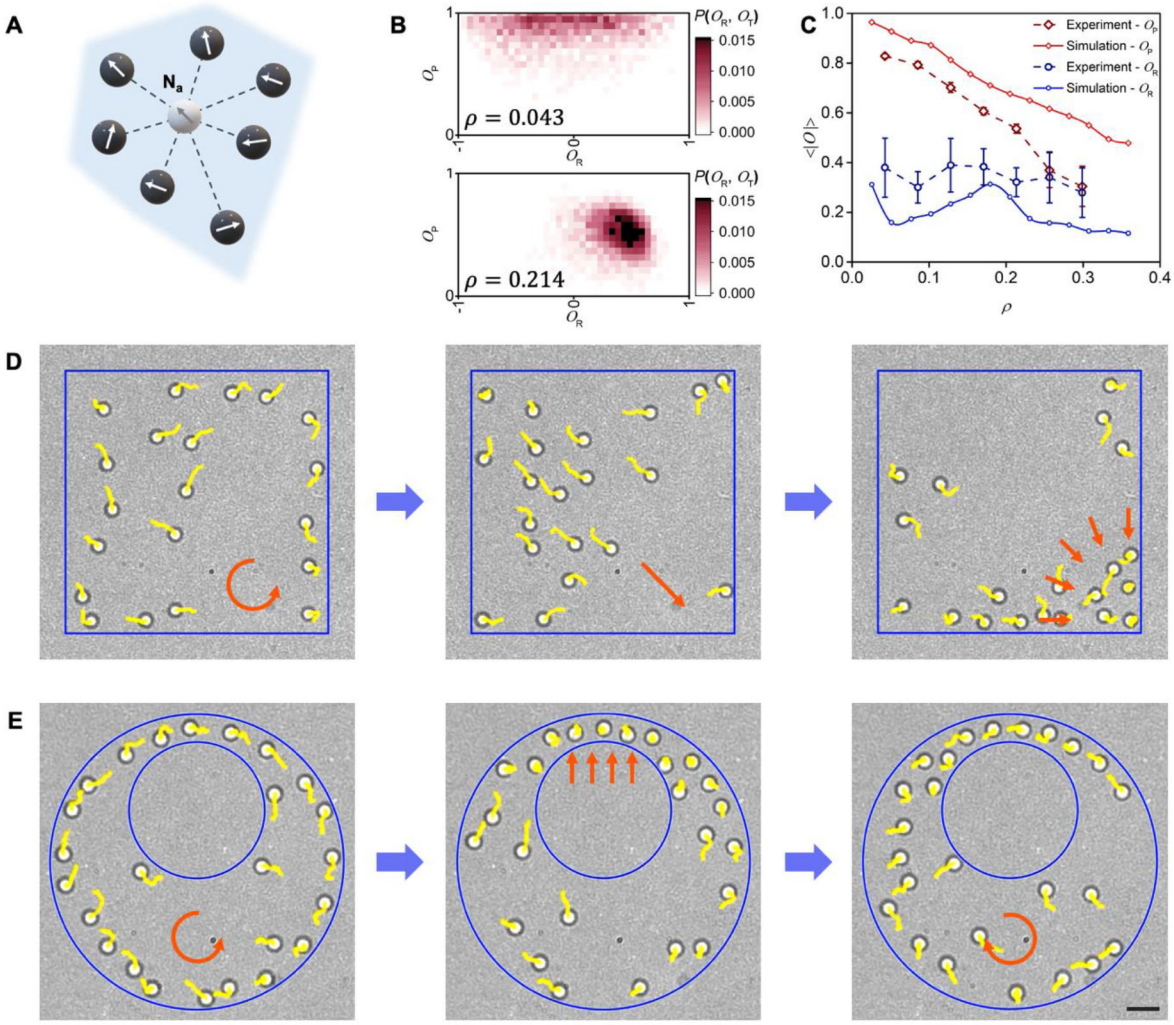

Figure 5. Variants in the topological-distance-based velocity alignment and different shapes of the confined geometry.

(A) Schematic of the topological-distanced-based velocity alignment. The center particle (white sphere) interacts with N_a of the nearest neighboring particles regardless of the metric distance. The white and grey arrows represent the moving direction of particles. (B) Histogram of the correlation between O_R and O_P under $\rho = 0.043$ (top) and $\rho = 0.214$ (bottom). (C) Simulations and experimental results of $\langle O_P \rangle$ (red) and $\langle |O_R| \rangle$ (blue) for the topological-distanced-based velocity alignment with $N_a = 7$. Optical images of (D) the rotating (left), polar (middle), and trapping (right) states of twenty active particles in a square-shape confined geometry, and (E) the anti-clockwise rotating (left), trapping (middle) and clockwise rotating (right) states of twenty-five active particles within an off-center ring-shape confined geometry. The orange arrows highlight the moving states of the collective structures. Scale bar: 5 μm. The sample sizes of experimental and simulated data are $n \geq 5$ and $n = 20$, respectively. The error bars indicate the standard deviation.